A large volume, portable, real-time PCR reactor†

Xianbo Qiu, Michael G. Mauk, Dafeng Chen, Changchun Liu and Haim H. Bau*

Received 19th May 2010, Accepted 26th August 2010
DOI: 10.1039/c0lc00038h

A point-of-care, diagnostic system incorporating a portable thermal cycler and a compact fluorescent detector for real-time, polymerase chain reaction (PCR) on disposable, plastic microfluidic reactors with relatively large reaction volume (ranging from 10 μL to 100 μL) is described. To maintain temperature uniformity and a relatively fast temperature ramping rate, the system utilizes double-sided heater that features a master, thermoelectric element and a thermal waveguide connected to a second thermoelectric element. The waveguide has an aperture for optical coupling between a miniature, fluorescent reader and the PCR reaction chamber. The temperature control is accomplished with a modified, feedforward, variable structural proportional-integral-derivative controller. The temperature of the liquid in the reaction chamber tracks the set-point temperature with an accuracy of ± 0.1 °C. The transition times from one temperature to another are minimized with controllable overshoots (< 2 °C) and undershoots (< 5 °C). The disposable, single-use PCR chip can be quickly inserted into a thermal cycler/reader unit for point-of-care diagnostics applications. The large reaction chamber allows convenient pre-storing of dried, paraffin-encapsulated PCR reagents (polymerase, primers, dNTPs, dyes, and buffers) in the PCR chamber. The reagents are reconstituted "just in time" by heating during the PCR process. The system was tested with viral and bacterial nucleic acid targets.

1. Introduction and background

Nucleic acid-based analysis utilizing enzymatic amplification is routinely employed in research, clinical diagnostics, and environmental testing.[1–3] The implementation of such methods in various microfluidic 'lab-on-a-chip' formats is well established.[4–6] For point-of-care diagnostics, microfluidic PCR offers substantial advantages when the PCR reactor is combined with sample processing and detection capabilities.

Most of the work to date on microfluidic-based polymerase chain reaction (PCR) reactors has focused on reducing the reaction volume of the PCR chamber to 1 μL or less. Small reaction volumes are desirable to enable fast cycling rates.[7–10] Also, in high-throughput operations in laboratories and in the pharmaceutical industry, the use of small volume PCR reactors reduces reagents' volume and cost. In point of care settings, however, there are many instances in which a large PCR reaction volume (ranging from 10 μL to 100 μL) is desirable. For example, the detection of pathogens in saliva and urine mandates large sample volumes due to the low concentration of the target analyte and the presence of PCR inhibitors. Furthermore, in low-cost systems for point of care diagnostics, it is difficult to achieve the precise flow control needed to work with sub-microliter volumes. Moreover, large PCR reaction chambers allow one to integrate into the reaction chamber (*i*) a nucleic acid binding phase ("membrane") to isolate and concentrate target nucleic acids[11] and (*ii*) encapsulated, dry-stored PCR reagents,[12] thereby, simplifying the flow control of the microfluidic system. Large reaction chambers also offer reduced surface-to-volume ratio which reduces the absorption of critical components (such as Taq DNA polymerase) to the chamber surface and reduced wall inhibition.

Unfortunately, PCR chambers with relatively large volumes present a few challenges. When the volume of the PCR reactor is smaller than 1–2 μL, one-sided heating of the chamber usually suffices to maintain a uniform temperature in the reaction chamber.[13,14] Larger reaction chambers may require more elaborate heating/cooling schemes. Previous reports by others[15,16] and by our group[12] indicate that the temperature uniformity and ramping rates of a ~10 μL PCR chip can be significantly improved when the PCR chamber is sandwiched between two heating/cooling elements.

Although PCR chips with relatively large volumes have been constructed with silicon and glass,[15,17–19] polymeric materials, such as polycarbonate (PC), polymethyl methacrylate (PMMA or 'acrylic'), polystyrene (PS), and cyclic olefin copolymer (COC), are preferred for disposable devices due to their lower cost, easier packaging, and ease of manufacturing. Problems with PCR temperature control are exacerbated, however, when the chips are made with low thermal conductivity polymeric materials. Furthermore, it is necessary to have relatively thick reaction chamber's walls (*i.e.*, >0.1 mm) to maintain the structural integrity of the comparatively large reaction chamber.

Although top-side and bottom-side heating/cooling are desirable to achieve uniform temperature and rapid temperature ramping, the placement of heaters on both sides of the chip restricts optical access to the reaction chamber for real time fluorescent monitoring of the PCR process. Some workers have solved this problem by using an optical waveguide placed in the plane of the chip.[20,21] This arrangement, however, increases cost of the chip and complicates its mating with an analyzer/reader.

In this paper, we provide engineering solutions for some of the challenges faced by the designer of large volume reaction

---

Department of Mechanical Engineering and Applied Mechanics, University of Pennsylvania, Philadelphia, USA. E-mail: bau@seas.upenn.edu

† Electronic supplementary information (ESI) available: Additional information. See DOI: 10.1039/c0lc00038h

chambers. We describe a thermal cycler and a control algorithm that provide excellent temperature control of relatively large reaction volumes (ranging from 10 to 100 μL) while facilitating direct optical access to the reaction chamber for real-time monitoring of the reaction progress with a compact, light-emitting diode (LED), confocal fluorescence-based detection device. We demonstrate that the performance of our device is compatible with that of benchtop instruments. The system is compatible with point-of-care diagnostics as it is configured for quick insertion and self-alignment of the disposable, single-use cassette in a portable actuator/reader instrument. In resource-poor settings, where ultra-low cost and simplicity are essential, the real-time fluorescent-based monitoring (described herein) can be replaced with a lateral flow strip that allows visual detection of the PCR products.[22]

2. Portable thermal cycler and optical reader system

Microfluidic PCR chips with large reaction volumes pose a challenge for temperature control. Fast temperature ramp rates and avoidance of excessive over- and under-shoot of temperature set-points (melting, primer annealing, and extension) are not only crucial for reducing total test time, but also for maintaining good performance of the PCR amplification process and minimizing artifacts such as non-specific hybridization and formation of primer-dimers at sub-optimal temperatures. For our application, we desire spatial temperature uniformity better than ± 0.5 °C over the reaction volume, a temperature ramping rate better than ± 6 °C/sec with minimal over/under-shoot (within 0.5 °C), as well as optical coupling for a statistically-significant fluorescence detection of at least 1000 copies of PCR amplicons.

To meet the above requirements, we developed a compact platform combining a thermal cycler and fluorescent reader for microfluidic-based PCR (Fig. 1). The cassette slides into a slot in the analyzer/reader and is sandwiched between two temperature-controlled surfaces. The bottom-side surface consists of the "master" thermoelectric (TE; HOT2.0-65-F2A, Laird Technologies, Cleveland, OH) element with an embedded type K thermocouple (0.075-mm diameter, Omega Engineering, Stamford, CT) located at the interface between the TE and the chip. The top-side temperature control is provided with a cantilevered metal plate ("thermal waveguide") made with a thin aluminum sheet (~ 250 μm, 9536K16, McMaster-Carr, Princeton, NJ) and equipped with a second embedded type K thermocouple that contacts the top side of the chip. The thermal waveguide provides a high thermal conductivity path from the "slaved," offset thermoelectric element (HOT2.0-65-F2A, Laird Technologies, Cleveland, OH) to the chip. The thermal waveguide presses against the chip to reduce thermal contact resistance, and it has a viewing port (2.5 mm diameter) to provide a direct optical path between the fluorescent reader and the PCR chamber. The schematic building blocks of the real-time PCR system are depicted in Fig. S1 (ESI†).

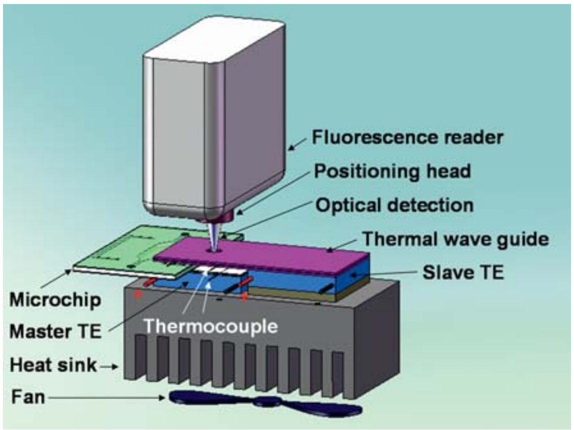

Fig. 1 A schematic depiction of the real-time PCR platform with a partially inserted microchip.

For real-time detection, we used a compact (64 mm × 49 mm × 23 mm), LED-based, confocal fluorescent reader (FLUO SENS SD 003 with handheld controller FLUO LOG, both from ESE GmbH, Germany), which interfaced with a computer through a USB port. The reader's excitation and emission wavelengths are, respectively, 460 nm and 520 nm. The manufacturer quotes a limit of detection of 10^{-9} moles of fluorescent molecules per μL sample.

To determine the optimal distance between the reader and the chip, we constructed a calibration polycarbonate chip and loaded it with purified DNA and SYTO-9 Green® fluorescent dye (Molecular Probes, Invitrogen, Eugene, OR). The reader's distance from the cassette was gradually varied to determine optimal reading distance. The fluorescent signal peaked when the reader's lens was between 2 and 4 mm from the chip's surface, with little variations in the signal intensity in this range.

3. Disposable, large-volume, polycarbonate microfluidic chip

A major component of point-of-care diagnostics systems is an inexpensive, single-use (disposable) microfluidic chip or cassette in which the sample is processed.[23] The chip mates with a portable instrument that provides temperature control, fluidic actuation and control (see ref. 41 for details), and excitation and detection of fluorescence emission. We made the chips with polymeric materials because of their low manufacturing cost, amenability to rapid prototyping, high-volume producibility, biocompatibility, and optical transparency.[24,25] Optical-quality plastic materials with a low autofluorescence are crucial for optimal detection by fluorescence and laser induced fluorescence techniques.[26] To reduce background fluorescence, we use a relatively thin (~ 125 μm) cover sheet to cap the reaction chamber.

The PCR chips used here were made by laminating three layers of polycarbonate sheets. Fig. 2(a) depicts the cross-section of the reaction chamber. The middle layer was machined from a 500-micron thick, polycarbonate sheet (85585K25, McMaster-Carr, Princeton, NJ) with a computer numerical controlled (CNC) milling machine (OM-2, Haas Automation, Oxnard, CA). Using acetonitrile (Fisher Scientific, Pittsburgh, PA), the milled middle layer was solvent bonded at room temperature with two, 0.125 mm thick, polycarbonate sheets (85585K72, McMaster-Carr) that formed the floor and ceiling of the chamber and conduits. Solvent bonding is preferred over thermal bonding since it avoids the deformation of the chamber's thin-walled floor and ceiling. Solvent bonding of primarily acrylic materials has been previously described.[42] This is a first demonstration of

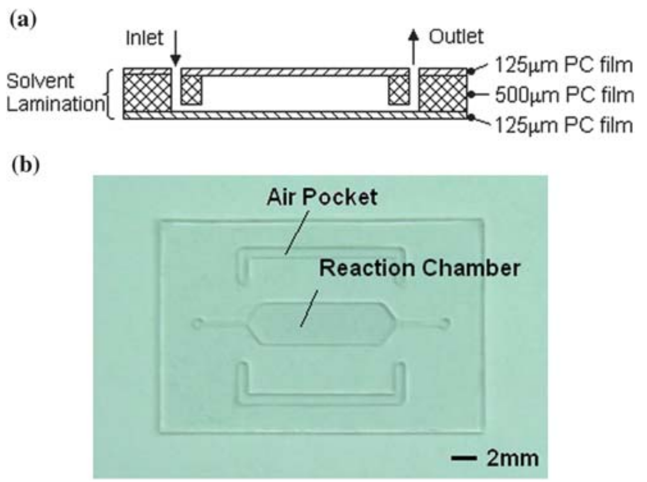

Fig. 2 The chip-based PCR chamber: (a) a cross-section, (b) a top view photograph of the single chamber microchip.

solvent bonding of polycarbonate. The bond is strong enough to withstand the elevated pressure that develops in the PCR reactor during the cycling process.

Fig. 2(b) shows a photograph of the solvent bonded chip comprised of a PCR reaction chamber (~25 µl), inlet and outlet conduits (500 µm width × 250 µm depth), and a rectangular heating zone (12 mm × 13 mm) defined by grooves that form air pockets to thermally insulate the reaction chamber. The grooves align with the perimeter of the master thermoelectric element and the thermal waveguide (see Fig. 1). The slots impede heat conduction in the plane of the chip and enhance the thermal response of the PCR reactor. The shallowness of the reaction chamber helps assure temperature uniformity in the reactor.[12]

4. Control algorithm

Most thermal controllers, including the ones used to control thermal cyclers, utilize proportional-integral-derivative (PID) algorithms.[27] Traditional PID controllers are, however, not optimal for PCR applications due to their relatively slow response time, which results from the need to avoid excessive temperature overshoot/undershoot.[28–34]

To improve the PCR control systems' dynamic response, we developed a modified feedforward, variable structural proportional-integral-derivative (MFVSPID) controller. This is a modified version of our earlier design, which combined the advantages of open-loop and closed-loop control to provide rapid heating with minimal overshoot.[29] The MFVSPID controller enhances the reactor's ramp rate by intentionally introducing temperature overshoots and undershoots.

A previous report[35] indicated that the ramping rate of an array of PCR chips can be improved by introducing a moderate overshoot (+2 °C) and undershoot (−2 °C). This strategy is, however, difficult to implement within the PID scheme since simple tuning of the proportional, integral, and derivative controller gains may lead to spurious temperature oscillations and integral action saturation ("windup"). As an alternative, we use a hybrid control strategy: feedforward control with variable structural PID control. Although the reactor's inside temperature could be provided by a "dummy" reaction chamber (analogous to the "active tube" control used in benchtop PCR thermal cyclers,[36,37] which utilize an instrumented reaction vial to monitor the actual reaction temperature), this proved unnecessary because the thermal waveguide's temperature closely tracked the temperature inside the reaction chamber, as we describe later in the paper.

To effectuate the double-sided heating scheme with master and slaved TE modules, a dual-loop control system was developed. One loop controls the master TE module, and the other loop controls the slave TE module that is coupled to the thermal waveguide. Both loops have their own thermocouples to provide the input signal. Fig. 3 depicts the block diagrams of both MFVSPID control loops. Each controller consists of a feedforward module and a variable structural PID module. The plant transfer function $G(s)$ for each control loop is determined by subjecting the TE module to a sequence of step changes in power and monitoring the response temperature as a function of time. We use the symbols r (r'), e (e'), and y (y'), to denote, respectively, the setpoint, the error, and the output signal of the master (slave) TE's control loop.

The feedforward, open-loop controller's signal consists of static and dynamic components:

$$u_{\mathrm{FF}} = u_{FF\text{-}static} \pm u_{FF\text{-}dynamic} \tag{1}$$

The static part of the u_{FF} is:[29]

$$u_{FF-static} = K_F(T_{setpoint} - T_{ambient}) + \Delta u_{FF} \tag{2}$$

The first term on the right hand side of eqn (2) represents the anticipated power needed to maintain the reactor's temperature at the set point temperature $T_{setpoint}$. This is the power needed to compensate for heat losses to the ambient. The term is a constant selected during the controller's tuning process to achieve reasonably fast ramp rates. To attain rapid response, the system operates with an overshoot/undershoot. The overshoot and undershoot amplitudes are controlled with the dynamic

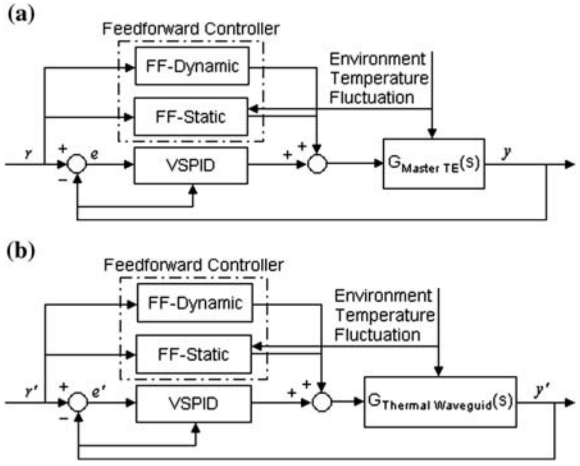

Fig. 3 A block diagram of the controller. (a) MFVSPID control loop for the master TE module, (b) MFVSPID control loop for the thermal waveguide module.

component $u_{FF\text{-}dynamic}$, which can be adjusted through on-line tuning.

The VSPID controller is a modified PID controller whose structure depends on the magnitude of the error signal. The VSPID signal

$$u_{VSPID}(k) = u_P(k) + H(e_1 - |e(k)|)[u_D(k) + H(e_2 - |e(k)|)u_I(k)] \tag{3}$$

where

$$u_P(k) = K_c e(k) \tag{4}$$

$$u_D(k) = -K_c \frac{T_d}{T}(y(k) - y(k-1)) \tag{5}$$

and

$$u_I(k) = \frac{K_c T}{T_i} \sum_{i=1}^{k} \left[\frac{e(i) + e(i-1)}{2}\right] \left[\frac{1}{1 + \frac{10{*}e(i)^2}{100^2}}\right] \tag{6}$$

In the above, k is the sampling point. The $u_P(k)$, $u_D(k)$, and $u_I(k)$ are, respectively, the VSPID proportional, derivative, and integral actions. K_c, T_d, and T_i are, respectively, the VSPID proportional, derivative, and integral controller gains. T is the length of the control cycle. $y(k)$ and e are, respectively, the system output and the control error. The partial derivative action, which only applied derivative action to the system output, was used to avoid derivative kick which may caused by the abrupt changes in setpoints. Trapezoidal integration is used to avoid sharp changes in integral action. The nonlinear adjustment of integral action $(1/(1 + 10{*}e(i)^2/100^2))$ is used to reduce overshoot.[38] $H(v)$ is the Heaviside function such that $H(v) = 0$ when $v < 0$ and $H(v) = 1$ when $v > 0$. The threshold errors e_1 and e_2 $(0 < e_2 < e_1)$ are selected during the controller's tuning process. When $|e(k)| > e_1$, the VSPID controller operates as a proportional controller. When $e_1 > |e(k)| > e_2$, the VSPID is a PD controller. When $e_2 > |e(k)|$, the VSPID is a PID controller. The integral gain of the VSPID controller enables the system to transition smoothly from the overshoot/undershoot state to the steady-state while avoiding controller saturation.

The schematic building blocks of the portable thermal cycler are discussed in section S2 of the electronic supplementary information (ESI†).

5. Results and discussion

5.1. Assessment of temperature control

To assess the performance of the thermal controller, we constructed an instrumented, calibration chip. The calibration chip has the same dimensions as the actual PCR chip and is equipped with a 75 μm diameter, type K thermocouple inserted at about the midheight of the reaction chamber's center. The calibration chip was sandwiched between the master TE and the thermal waveguide (Fig. 1). The experiments were carried out in a room at ~ 20 °C. When the reaction chamber temperature was set to 94.0 °C, single-sided heating with the master TE resulted in a steady state temperature difference of ~ 2.5 °C between the master TE's surface and the inside of the reaction chamber. When double-sided heating was used (Fig. 1), the temperature difference between the master TE's surface and the reaction chamber was reduced to about 0.2 °C. Another calibration chip with three thermocouples inserted at the bottom, midheight, and top of the reaction chamber indicated that the temperature nonuniformities within the chamber were smaller than ± 0.3 °C.

The thermal time-response of the system was tested in a separate set of experiments. Fig. 4(a) depicts the set temperature (thick solid line), the master TE's temperature (dotted line), the thermal waveguide's temperature (dashed line), and the reaction chamber's temperature (thin solid line) as functions of time within one PCR cycle. All the above measurements were carried out with the calibration chip. Fig. 4(b) depicts the set temperature (solid line), the master TE's temperature (dotted line), and the thermal waveguide's temperature (dashed line) as functions of time during the 40 PCR cycles.

With a master TE temperature overshoot smaller than 2 °C and undershoot smaller than 5 °C, the system achieved a heating rate of approximately 4 °C/s and a cooling rate of approximately 6 °C/s. The overshoot and undershoot in the reaction chamber's temperature were, respectively, smaller than 0.2 °C and 0.15 °C. The steady-state setpoint was tracked with an accuracy of ± 0.1 °C. The ramp rate was not significantly attenuated as the temperature approached its setpoint, which ultimately resulted in faster transitions between the various set points of one cycle. Witness that the reaction chamber's temperature followed closely

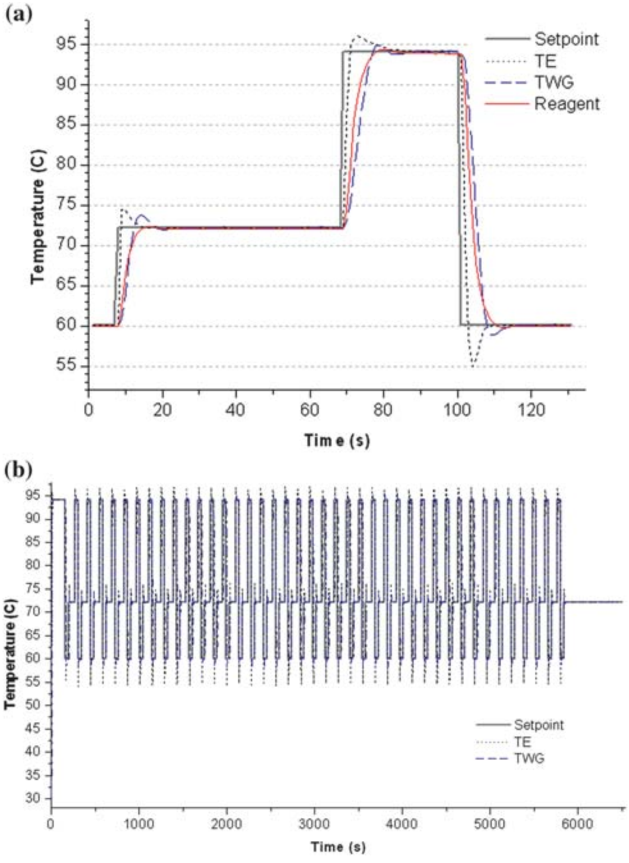

Fig. 4 The set temperature (thick solid line), the master TE's temperature (dotted line), the thermal waveguide's temperature (dashed line), and reaction chamber's temperature (thin solid line) are depicted as functions of time during one cycle of the MFVSPID controller (a), and during the entire 40-cycle (b).

the thermal waveguide's temperature during ramp up and ramp down and more so during steady-state conditions. For this reason, we were able to record the dwell time for each PCR step based on the thermal waveguide's temperature.

5.2. PCR performance with purified λ-bacteriophage genomic DNA

To demonstrate that our portable PCR reactor's performance is comparable to commercial benchtop reactors, we used a commercial PCR test kit (Takara Biosystems, Shiga, Japan) with λ-bacteriophage genomic DNA (48 kbp) as a template and primers for a 1000-bp amplicon. The use of a purified template allowed us to assess the performance of the PCR reactor itself, independent of factors related to the possible presence of PCR inhibitors and other issues associated with the sample preparation.

The PCR reaction mix was comprised of one IllustraPureTaq™ "Ready-to-Go" PCR bead (GE Healthcare, Piscataway, NJ) containing 2.5 units of Taq DNA polymerase, 10 mM Tris-HCl, 50 mM KCl, 1.5 mM $MgCl_2$, 200 μM dNTPs in carbohydrate stabilizers and bovine serum albumin (BSA); 20 μM primers; 1 fg λ DNA template (20 copies); 0.5 μl PEG 8000 (polyethylene glycol, avg. MW = 8000; Sigma Aldrich); 2 μM SYTO-9 Green™ DNA-intercalating fluorescent dye (Invitrogen Molecular Probes, Eugene OR); and molecular-biology grade water. The PCR components were prepared and mixed on the benchtop and pipetted into the PCR chamber of the chip. The chip outlet and inlet ports were sealed with ~3 mm × ~3 mm adhesive aluminum foil PCR tape (Microseal 'F', Bio-Rad Laboratories, Hercules, CA). Following the reagents manufacturer's recommendations, the thermal cycling program starts with a 94 °C initial denaturation for 1 minute, followed by 45 cycles (denaturization: 94 °C, 30 s; annealing 60 °C, 30 s; extension 72 °C, 1 min), and ended with a final extension of 72 °C for 10 minutes. During thermal cycling, the reaction was monitored in real time with the fluorescence reader and the fluorescence intensity was recorded during the extension step of each cycle. No-template (negative) controls were also run in the chips to ensure the absence of false positives. For comparison, both a positive control run with 1 fg λ DNA template and a negative control run (0 fg) were performed on benchtop with a commercial PCR instrument (Techne Incorporated, Princeton, NJ). For verification, the PCR products from both the chip and the benchtop were run on a 1.5% agarose gel (with 1% ethidium bromide stain) along with Roche Marker VIII ladder, and the gel was imaged with a fluorescence gel viewer. The experiment was repeated multiple times with similar results.

Fig. 5 depicts the fluorescence intensity of the signal (during the extension step) for 1 fg of λ DNA (20 copies) (up directed solid triangles) and for the no-template control (NTC, down directed solid triangles) as a function of the cycle number. Images of gel electrophoresis of PCR amplifications are provided in the inset. Lanes 1 and 4 are the Marker VIII ladders. Lanes 2 and 3 correspond, respectively, to the microchip's PCR products with 1 fg λ DNA template (20 copies) and the no-template negative control (NTC). Lanes 5 and 6 correspond, respectively, to the benchtop's PCR products with 1 fg λ DNA template and the no-template negative control. In the presence of 1 fg λ DNA template, the fluorescent signal peaks at about 27 cycles. The gel electropherogram (lane 2) features a strong band at 1000bp consistent with the presence of the desired amplicons. The electropherogram also shows the presence of smaller, double stranded DNA molecules of approximately 60 bp. We suspect that the secondary, diffuse band at ~60bp is due to the formation of primer dimers (possibly resulting from a suboptimal design of the primers). Formation of primer-dimers is a common problem to many PCR amplification processes. The negative (no template) control also provided a fluorescent signal, albeit of significantly lower intensity than the positive control. This threshold or take-off signal appeared after about 35 cycles. Examination of the corresponding electropherogram (lane 3) reveals the lack of amplicon band at 1000bp, consistent with the absence of a template, and the presence of a band at ~60 bp (lane 3). We attribute the secondary band (at ~60 bp) to the formation of primer dimers, which apparently were also responsible for the appearance of the real-time, fluorescent signal generated by the negative control. Witness that the electropherogram (lane 2) of the chip-based amplicons is very similar to the electropherogram (lane 5) of the benchtop machine. One can conclude that (i) the formation of primer-dimers is not an artifact of our device but an intrinsic characteristic of the assay and (ii) the performance of the chip-based PCR is equivalent to that of a benchtop instrument.

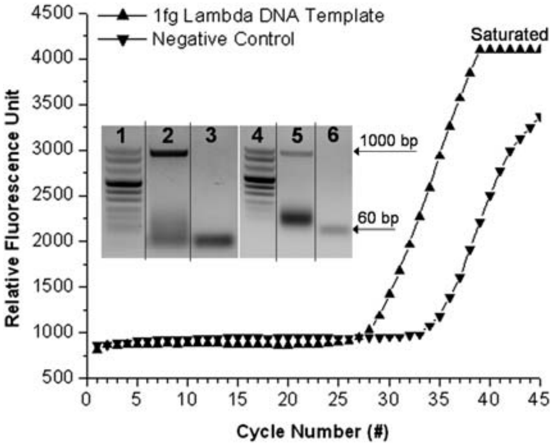

Fig. 5 Microchip real-time PCR with λ DNA template. The detected fluorescent intensity (measured during the extension step) is indicated as a function of the cycle number. The up directed and downward directed triangles correspond, respectively, to 1 fg (~20 copies) template and 0fg (negative, no template control). The inset features the agarose gel (1.5%) electropherogram of the PCR products. Lanes 1 and 4 are the Roche Marker VIII ladders. Lanes 2 and 3 correspond, respectively, to the microchip's PCR products of 1 fg λ DNA template (20 copies) and the no-template control (NTC). Lanes 5 and 6 correspond, respectively, to the benchtop's PCR products of 1 fg λ DNA template and the non-template control amplified in a commercial PCR instrument.

A number of strategies are available to discriminate between primer-dimer formation and true target amplification. First, a test could be deemed positive only when the signal threshold occurs before a predetermined number of PCR cycles (*i.e.*, 35 in Fig. 5). Alternatively, one can produce a post-amplification melting curve to obtain the melting temperatures of the PCR product(s) and infer their base-pair lengths, permitting one to distinguish between target amplicons, spurious primer-dimers, and other unintended amplification products.[39] Yet another strategy to minimize false positives is through the use of molecular beacons such as TaqMan that light up only upon binding to a predetermined sequence.[40]

5.3. PCR detection of gram-positive bacteria DNA

The utility of the microfluidic PCR system for detecting bacterial pathogens was demonstrated by amplifying genomic DNA from gram-positive *Bacillus cereus*. *B. Cereus* serves as a safe surrogate for anthrax and represents a typical bacterial target for amplification, especially when the microfluidic PCR reactor is integrated with components for sample concentration lysis and nucleic acid isolation in an autonomous, sample-to-report system.[22,41]

Genomic DNA was isolated from *B. Cereus* (ATTC, Culture Type 6464, designation NRS 210) cultures grown overnight and harvested in log phase. The bacterial cell concentrations in the culture stocks were counted with a hemacytometer. Genomic DNA was isolated from the *B. Cereus* culture stocks using the Qiagen DNEasy™ (Tissue) silica-chaotrope method spin-column kit. The concentration of isolated DNA was measured using a NanoDrop ND-1000 spectrophotometer and a fluorescence assay with Picogreen dye. The PCR reaction mix was similar to the one described in section 5.2, albeit with different primers. The *B. cereus*-specific primers, 5′biotin TCT CGC TTC ACT ATT CCC AAG T-3′ and 5′dioxigenin-AAG GTT CAA AAG ATG GTA TTC AGG-3′ (0.3 μM, Eurofins MWG Operon, Huntsville, AL) yielded a 305-bp amplicon. The primers were conjugated with biotin and dioxigenin to facilitate lateral flow-based detection as an alternative to real-time fluorescence measurement; for a description of the lateral flow-based detection, see reference 41. The thermal cycling program started with a 2 min 94 °C initial denaturization step, followed by 40 cycles (denaturization 94 °C, 15s, annealing 55 °C, 18s, and extension 68 °C for 23 s), and concluded with a final extension of 68 °C for 2 min.

Fig. 6 depicts the real-time fluorescence intensity as a function of cycle number *n* for PCR amplifications of samples containing 3×10^5 (solid squares), 3×10^3 (up directed triangles), and 0 (negative control, down directed triangles) copies of *B. cereus* genomic DNA. The gel electropherograms of the PCR amplificons are shown in the inset in Fig. 6. Lane 1 is the Marker VIII ladder. Lanes 2, 3, and 4 correspond, respectively, to 3×10^5, 3×10^3, and 0 copies in the original sample. When there were 3×10^5 and 3×10^3 copies in the sample, the fluorescent signal threshold occurred at 17 and 27 cycles, respectively. The electropherograms exhibit well-defined bands for the expected 305-bp PCR product. The negative sample exhibited neither fluorescent signal nor band. In contrast to the experiments with the λ DNA (section 5.2), the *B. cereus* assay did not exhibit any significant primer-dimer formation. We surmised that the *B. cereus* primers are designed to be orthogonal to each other to discourage primer dimer formation. Witness also that the slope of the fluorescent intensity *versus* the number of cycles in Fig. 6 is lower than in Fig. 5, indicating a lower PCR amplification efficiency, which may be due to the presence of polymerase inhibitors such as traces of ethanol and salts from spin-column isolation steps. The electropherograms of Fig. 6 are similar to electropherograms obtained with benchtop experiments (not shown).

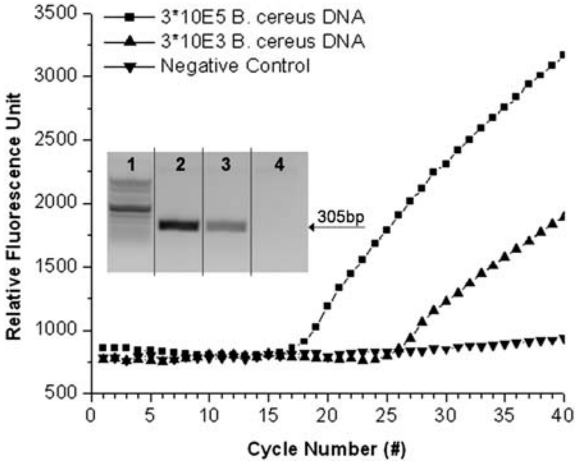

Fig. 6 Real-time PCR intensity as a function of cycle number. The template is gram-positive *B. cereus* DNA. The squares, up pointing triangles, and down pointing triangles correspond, respectively, to 3×10^5, 3×10^3, and 0 (negative control) template molecules. The inset is an agarose gel (1.5%) electropherogram of the PCR products. Lane 1 is a Marker VIII ladder. Lanes 2, 3, and 4 correspond, respectively, to the microchip PCR products for starting template amounts of 3×10^5 copies, 3×10^3 copies, and negative control.

5.4. PCR chips with pre-loaded, dry-stored reagents

Pre-storage of PCR reagents in the chip greatly simplifies its operation. In prior work,[11] we developed an in-situ storage technique that consists in encapsulating the PCR reagents in paraffin and pre-loading the encapsulated reagents into the PCR reaction chamber at the time of the chip's fabrication. The paraffin encapsulation layer preserves the dried reagents and protects them from dissolution prior to the thermal cycling. When the PCR chamber is heated above 60–65 °C, the paraffin melts and migrates to the periphery of the reaction chamber due to surface tension effects and buoyancy forces. The reagents are released and reconstituted in the liquid containing the DNA template target, such as the PCR-compatible buffer used to elute isolated DNA from the nucleic acid binding membrane. Here, we show that our PCR reagent dry storage, pre-loading method and the consequent presence of paraffin in the reaction chamber impede neither amplification nor real-time fluorescence monitoring of the PCR reaction. The relatively large volume of reaction chamber greatly simplifies the *in-situ* storage.

For this experiment, we prepared a PCR mixture similar to that used for the λ DNA tests (section 5.2) augmented with 50% additional Taq DNA polymerase. We used the extra quantity of Taq DNA polymerase to compensate for the possible loss of enzyme activity during our primitive dry storage, which consisted of leaving the PCR reagents to dry at room conditions. It is likely that more sophisticated drying techniques such as vacuum freeze-drying (lyophilization) will not require us to increase the amount of enzyme. We also added to the PCR mix preservatives extracted from a well of a Sample-Gard® (Biomatrica, San Diego, CA). The preservatives stabilized the enzyme and primers and, as an extra benefit, contained a PCR-compatible red dye that indicated the location of dried reagents during the wax encapsulation step and helped us monitor the integrity of the paraffin encapsulation during buffer flow though the reaction chamber. A colored PCR product with a characteristic red shade indicates the release of the dried reagents during the PCR reaction.

A solution of the PCR mix was placed in an open PCR chamber (prior to solvent bonding of the chamber lid) and left to dry in air. The chip was then placed on a hotplate at 65 °C, and a 1 mm diameter ball of PCR-compatible paraffin (Ampliwax® PCR Gem, Applied Biosystems, Foster City, CA) was melted over the dried PCR mix, and allowed to re-solidify. The top layer of the reaction chamber (Fig. 2) was then solvent-bonded at room temperature to seal the reaction chamber. The sealing process and any residual solvent appear to have no significant effect on the PCR amplification.

Next, the sample containing λ-DNA template (suspended in water) mixed with 2 μM SYTO-9 Green™ DNA-intercalating fluorescent dye (Invitrogen Molecular Probes, Eugene OR) was added to the chip, and the chip was sealed with tape and thermally cycled. The fluorescent signal was obtained during the extension step of each cycle. Fig. 7 depicts the fluorescence intensity of the signal for 100 fg of λ DNA (2000 copies) (up directed solid triangles) and for the no-template control (NTC, down directed solid triangles) as functions of the cycle number. The gel electrophoresis of PCR amplifications is provided in the inset. Lane 1 is a Marker VIII ladder, and lanes 2 and 3 correspond, respectively, to the microchip's PCR products of 100 fg λ DNA template and the no-template control (NTC). The fluorescent intensity curve increases above the background level at about 23 cycles. This threshold is lower than the one observed in Fig. 5 reflecting the fact that the number of target molecules here is larger than in Fig. 5. The gel electropherogram (lane 2) features a strong band at 1000bp consistent with the presence of the target amplicons. The results obtained with the chip experiments are comparable to benchtop results (not shown) in which the paraffin encapsulated PCR mix was added to a PCR reaction tube and the amplification was performed using a real-time PCR instrument (Chromo4, Bio-Rad Laboratories, Hercules, CA 94547). Interestingly, the formation of primer-dimers appears to be less of a problem in this experiment than in experiments carried out with lower target concentrations (section 5.2 and Fig. 5). Perhaps at higher target concentrations, more of the primers are consumed in the DNA amplification and fewer are available for primer-dimer formation.

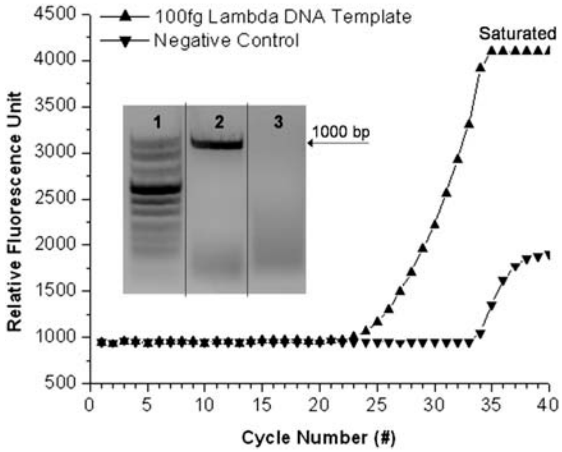

Fig. 7 Microchip real-time PCR with λ DNA template in the microchip. The detected fluorescent intensity (measured during the extension step) is depicted as a function of the cycle number. The up-directed and downward-directed triangles correspond, respectively, to 100 fg (~2000 copies) template and negative (no template) control. The inset features the agarose gel (1.5%) electropherograms of the PCR products. Lane 1 is a Marker VIII ladder, and lanes 2 and 3 correspond, respectively, to the microchip PCR products for 100 fg λ DNA template and the no-template control (NTC).

The experiments reported here and related work by our group[12] show that the paraffin encapsulation is compatible with chip PCR and that the melted paraffin does not interfere with real-time fluorescence measurements.

6. Conclusions and outlook

We have described a portable, inexpensive thermal cycler and chip with relatively large reaction volume (> 10 μL) for PCR amplification and real time monitoring and a thermal controller that minimizes the adverse effects of the relatively large thermal mass. Much of the recent efforts of the research community have focused on reducing the PCR chamber's volume to reduce cycle time. In many practical clinical settings however, it is necessary to accommodate relatively large sample volumes. We encountered such a need when developing systems to detect microorganisms in saliva.[41] Large volumes of saliva samples are readily available, but they contain a relatively low number of target pathogens. Large PCR reaction volumes can accept larger elutions from solid-state membranes and are less sensitive to the unavoidable presence of PCR inhibitors. Other advantages of large volume PCR reactors include flexibility and enough capacity in integrating PCR with microfluidic sample preparation steps such as integration of a solid state nucleic acid isolation membrane into the reaction chamber itself[11] and dry storage of PCR reagents with just-in-time release[12] and improved reliability due to better tolerance of air bubbles and other flow anomalies. Large volume reactors also provide increased sensitivity for real time detection and easier interfacing with the optics for fluorescent detection.

The main disadvantage of large volume reactors is their relatively large thermal mass. We have shown that the spatial temperature uniformity and ramping speeds can be enhanced by using two-sided heating/cooling and a specialized control algorithm with fine-tuned overshoot and undershoot. In this work, we used commercially-available reagents according to protocols recommended by the manufacturer, to demonstrate that the performance of our portable device is comparable with that of benchtop equipment. The broad temperature plateaus of Fig. 4(a) suggest, however, that the cycling time can be significantly reduced with appropriate optimization specific to various clinical applications.

To enable real-time monitoring of the amplification process, we used a thermally conducting "thermal waveguide" with a viewing port aperture. The thermal waveguide forms a flexible cantilever over the reactor chamber and can act as a spring to reduce thermal contact resistance between the chip and the heating elements and facilitates easy self-aligned insertion and withdrawal of the chip from the thermal cycler/fluorescent reader instrument, facilitating point-of-care operation.

To demonstrate the capabilities of the device, we carried out a sequence of tests with λ DNA and DNA isolated from *B. cereus*. Our device demonstrated similar capabilities to those of benchtop, laboratory-based instruments. In the case of the λ DNA experiments, we observed both in our device and in benchtop experiments false-positive real-time signals. We attribute these signals to the formation of primer dimers. This is a known problem in biotechnology and is not specific to our apparatus. Among other means, false positives can be discounted with the aid of melting curves that allow one to estimate the length of the amplicon[39] or through the use of specific TaqMan probes[40] or other sequence specific beacons which emit fluorescent signals only upon binding to their intended target.

We have also demonstrated that we can pre-store paraffin-encapsulated PCR reagents inside the PCR chamber. As the chamber is heated, the paraffin melts and moves out of the way. The reagents are released and hydrated just in time when needed. Our experiments indicate that the paraffin does not interfere with either the amplification process or with the real time monitoring. The durability of the paraffin encapsulation method was reported elsewhere.[12]

The PCR module described in this work will be integrated into a comprehensive nucleic acid detection chip that carries all the necessary steps from sample introduction to results including, among other things lysis, nucleic acid isolation, concentration, and purification, thermal cycling, and detection.[41]

Acknowledgements

The work was supported by NIH/NIDCR Grant U01DE017855.

References

1 R. K. Saiki, S. Scharf, F. Faloona, K. B. Mullis, G. T. Horn, H. A. Erlich and N. Arnheim, *Science*, 1985, **230**, 1350–1354.
2 T. Notomi, H. Okayama, H. Masubuchi, T. Yonekawa, K. Watanabe, N. Amino and T. Hase, *Nucleic Acids Res.*, 2000, **28**, 63e.
3 T. Uemori, H. Mukai, O. Takeda, M. Moriyama, Y. Sato, S. Hokazono, N. Takatsu, K. Asada and I. Kato, *J. Biochem.*, 2007, **142**, 283–292.
4 C. Zhang, J. Xu, W. Ma and W. Zheng, *Biotechnol. Adv.*, 2006, **24**, 243–284.
5 G. Huang, C. Han, X. Yang, J. Zhu, S. Xu and C. Deng, *J. Innovative Opt. Health Sci.*, 2008, **1**, 257–265.
6 J. Wang, Z. Chen, P. L. A. M. Corstjens, M. G. Mauk and H. H. Bau, *Lab Chip*, 2006, **6**, 46–53.
7 H. Kim, S. Vishniakou and G. W. Faris, *Lab Chip*, 2009, **9**, 1230–1235.
8 J. Lee, K. Cheong, N. Huh, S. Kim, J. Choi and C. Ko, *Lab Chip*, 2006, **6**, 886–895.
9 J. S. Marcus, W. F. Anderson and S. R. Quake, *Anal. Chem.*, 2006, **78**, 956–958.
10 A. Gulliksen, L. Solli, F. Karlsen, H. Rogne, E. Hovig, T. Nordstrøm and R. Sirevåg, *Anal. Chem.*, 2004, **76**, 9–14.
11 J. Kim, M. G. Mauk, D. Chen, X. Qiu, J. Kim, B. Gale and H. H. Bau, *Analyst*, 2010, **135**, 2408.
12 J. Kim, D. Byun, M. G. Mauk and H. H. Bau, *Lab Chip*, 2009, **9**, 606–612.
13 P. N. Ngatchou, M. R. Holl, C. H. Fisher, M. S. Saini, J. Dong, T. T. H. Ren, W. H. Pence, D. L. Cunningham, S. E. Moody, D. A. Donaldson and D. R. Meldrum, *IEEE Trans. Autom. Sci. Eng.*, 2006, **3**, 141–151.
14 N. Ramalingam, H. Liu, C. Dai, Y. Jiang, H. Wang, Q. Wang, K. Hui and H. Gong, *Biomed Microdevices*, 2009, DOI: 10.1007/s10544-009-9318-4.
15 M. A. Northrup, B. Benett, D. Hadley, P. Landre, S. Lehew, J. Richards and P. Stratton, *Anal. Chem.*, 1998, **70**, 918–922.
16 J. Khandurina, T. E. McKnight, S. C. Jacobson, L. C. Waters, R. S. Foote and J. M. Ramsey, *Anal. Chem.*, 2000, **72**, 2995–3000.
17 N. C. Cadya, S. Stelickb, M. V. Kunnavakkamc and C. A. Battd, *Sens. Actuators, B*, 2005, **107**, 332–341.
18 H. Nagai, Y. Murakami, K. Yokoyama and E. Tamiya, *Biosens. Bioelectron.*, 2001, **16**, 1015–1019.
19 I. Schneegaß, R. Bräutigam and J. M. Köhler, *Lab Chip*, 2001, **1**, 42–49.
20 Z. Wang, A. Sekulovic, J. P. Kutter, D. D. Bang and A. Wolff, *Electrophoresis*, 2006, **27**, 5051–5058.
21 C. G. J. Shabmueller, J. R. Pollard, A. G. R. Evans, J. S. Wilkinson, G. Ensell and A. Brunschweiller, *J. Micromech. Microeng.*, 2001, **11**, 329–333.
22 Z. Chen, M. G. Mauk, J. Wang, W. R. Abrams, P. L. A. M. Corstjens, R. S. Niedbala, D. Malamud and H. H. Bau, *Ann. N. Y. Acad. Sci.*, 2007, **1098**, 429–436.
23 C. Liu, X. Qiu, S. Ongagna, D. Chen, Z. Chen, W. R. Abrams, P. L. Corstjens and H. H. Bau, *Lab Chip*, 2009, **9**, 768–776.
24 X. Qiu, J. A. Thompson, Z. Chen, C. Liu, D. Chen, S. Ramprasad, M. G. Mauk, S. Ongagna, C. Barber, W. R. Abrams, D. Malamud, P. L. A. M. Corstjens and H. H. Bau, *Biomed. Microdevices*, 2009, **11**, 1175–1186.
25 A. Griebel, S. Rund, F. Schönfeld, W. Dörner, R. Konrad and S. Hardt, *Lab Chip*, 2004, **4**, 18–23.
26 A. Piruska, I. Nikcevic, S. H. Lee, C. Ahn, W. R. Heineman, P. A. Limbacha and C. J. Seliskar, *Lab Chip*, 2005, **5**, 1348–1354.
27 K. J. Åström and T. Hägglund, *Control Eng. Pract.*, 2001, **9**, 1163–1175.
28 V. N. Hoang, G. V. Kaigala and C. J. Backhouse, *Lab Chip*, 2008, **8**, 484–487.
29 X. Qiu, J. Yuan and Z. Wang, *Chin. J. Chem. Eng.*, 2006, **14**, 200–206.
30 A. I. K. Lao, T. M. H. Lee, I. Hsing and N. Y. Ip, *Sens. Actuators, A*, 2000, **84**, 11–17.
31 M. P. Dinca, M. Gheorghe, M. Aherne and P. Galvin, *J. Micromech. Microeng.*, 2009, **19**, 065009–15.
32 Q. Chen, Z. Wu, Y. Lin, *Proceedings of the IEEE International Conference on Systems, Man, and Cybernetics*, San Diego, 1998.
33 C. Liao, G. Lee, H. Liu, T. Hsieh and C. Luo, *Nucleic Acids Res.*, 2005, **33**, e156.
34 US Pat., 0 248 534 A1, 2008.
35 Q. Wang and H. Gong, *Proceedings of SPIE*, Maspalomas, 2003.
36 K. Phrases, *Thermo Electron Research Group Report*, 2003, **1**.
37 J. Wang and N. Zhang, *Proceedings of 7th IEEE/ACIS International Conference on Computer and Information Science*, Portland, 2008.
38 *National Instruments, LabView PID control toolset user manual*, November 2001 edn., 2001, (ch. 2), pp. 2–5.
39 N. Ramalingam, H. Liu, C. Dai, Y. Jiang, H. Wang, Q. Wang, K. M. Hui and H. Gong, *Biomed. Microdevices*, 2009, **11**, 1007–1020.
40 K. Wong, R. Lyddon and S. Dracheva, *Anal. Biochem.*, 2009, **390**, 173–180.
41 D. Chen, M. G. Mauk, X. Qiu, C. Liu, J. Kim, S. Ramprasad, S. Ongagna, W. R. Abrams, D. Malamud, P. L. A. M. Corstjens and H. H. Bau, *Biomed. Microdevices*, 2010, **12**, 705–719.
42 US Pat., 7, 608, 160 B2, 2009.